Supplementary Information

Pyrophosphate-stabilised amorphous calcium carbonate for bone substitution: toward a doping-dependent cluster-based model

Marion Merle[1], Jérémy Soulié[1], Capucine Sassoye[2], Pierre Roblin[3], Christian Rey[1], Christian Bonhomme[2], Christèle Combes[1,*]

1. CIRIMAT, Université de Toulouse, CNRS, TOULOUSE INP - ENSIACET, Toulouse, France
2. Sorbonne Université, CNRS, LCMCP, Paris, France
3. LGC, CNRS, Université de Toulouse, 118 route de Narbonne Bâtiment 2R1, Toulouse, France

A. Pyrophosphate precursor

The XRD diagram and FTIR spectrum of the sodium pyrophosphate precursor are presented Figure S1. The attribution of the FTIR bands is done according to Gras's work.[1]
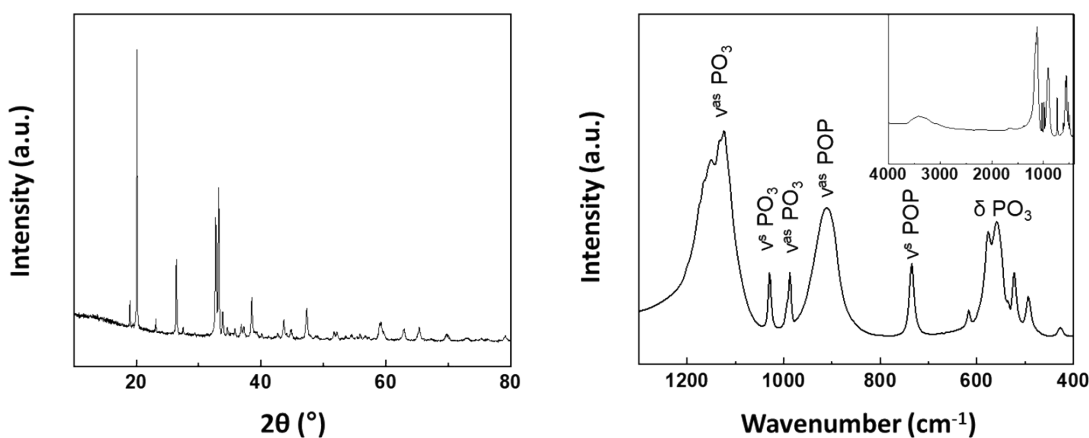

Figure S1: XRD diagram (left) and FTIR spectrum (right) of the synthesised sodium pyrophosphate precursor used for the synthesis of the zPyACC powders.

B. FTIR spectroscopy analysis of the ^{13}C-enriched zPyACC samples

A shift of the carbonate vibration bands in FTIR spectrum (Figure S2) confirmed the quasi-total enrichment in ^{13}C of the powder. Indeed, the ν_2CO_3 at 865 cm^{-1} in 10PyACC and in 5PyACC was totally shifted at 838 cm^{-1} for 10PyACC13 and 5PyACC13 samples. This shift (experimental ratio of 0.969) is in accordance with Rey *et al.*,[2] stating that for the ν_2CO_3 vibration the line position ratio is 0.9686. It is also in agreement with the shift obtained by Xu *et al.*[3] for the ν_2 vibration of 100% ^{13}C enriched calcite ($\nu_2{}^{12}CO_3$ at 877 cm^{-1} and $\nu_2{}^{13}CO_3$ at 850 cm^{-1}).
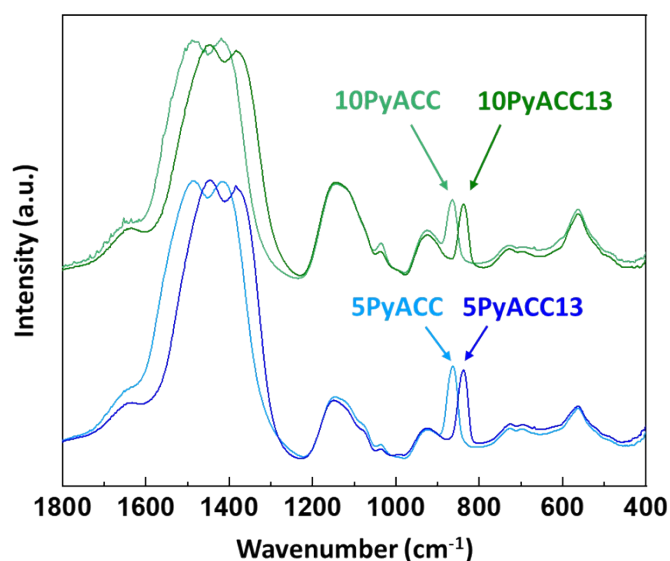
Figure S2: FTIR spectra of the 10PyACC and 5PyACC and their corresponding ^{13}C enriched powders, 10PyACC13 and 5PyACC13 respectively.

C. Raman spectra of the zPyACC powders

Raman spectroscopy analysis was done using a Raman Labram HR 800 confocal microscope Horiba Jobin Yvon, with a continuous 532 nm argon diode laser and a power of 8 mW. Samples were observed with a BX 41 Olympus microscope equipped with a x100 lens, conferring a spatial resolution of 0.7 μm and an axial resolution (penetration length) of 2.6 μm. Spectra were collected with a spectral resolution of 1.5 cm^{-1}, thanks to the grating of 600 lines per mm. Each spectrum was recorded with an integration time of 60 s and 3 accumulations.

The vibration bands corresponding to the carbonate and pyrophosphate groups can be observed in the Raman spectra (Figure S3).[4,5] The major carbonate band, corresponding to the symmetric stretching vibration v_1CO_3, at 1085 cm^{-1} in the calcite (0PyACC) is shifted to 1081 cm^{-1} in ACC. The smaller bands associated to v_3CO_3 and v_4CO_3 are respectively at 1437 cm^{-1} and 712 cm^{-1} in calcite, but much less pronounced or undetectable in ACC as the lattice bands below 400 cm^{-1} which are also not detectable in ACC. Concerning the pyrophosphate, the main band, attributed to v^sPO_3 and located at 1040 cm^{-1}, is characteristic of amorphous calcium pyrophosphate (aCPP).[1] The v^sPOP vibration, at 732 cm^{-1}, is also attributed to aCPP.
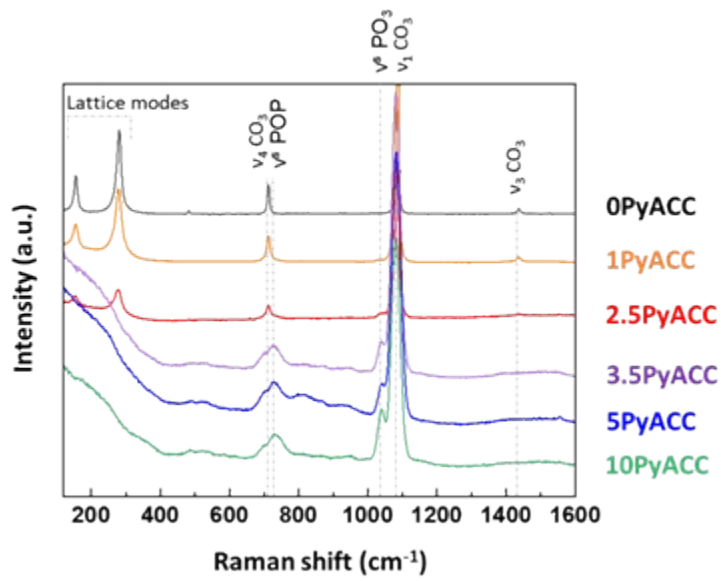
Figure S3: Raman spectra of the various zPyACC synthesised powders, with the associated carbonate and pyrophosphate vibrations identified.
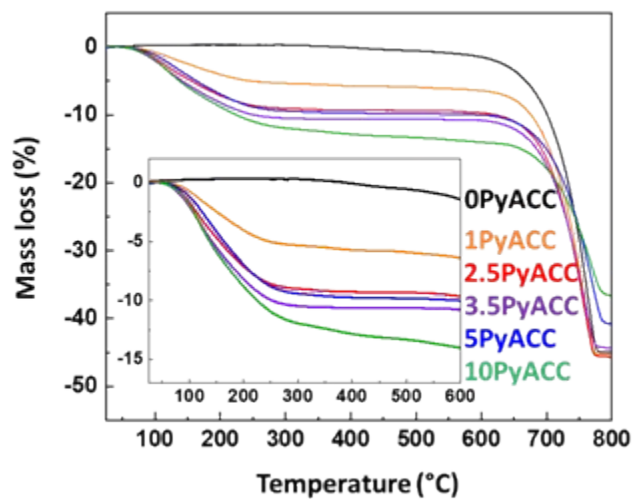
D. Thermogravimetric analysis

Figure S4: TGA curves of the zPyACC samples heated from 25°C to 800°C in air at a rate of 5°C/min.
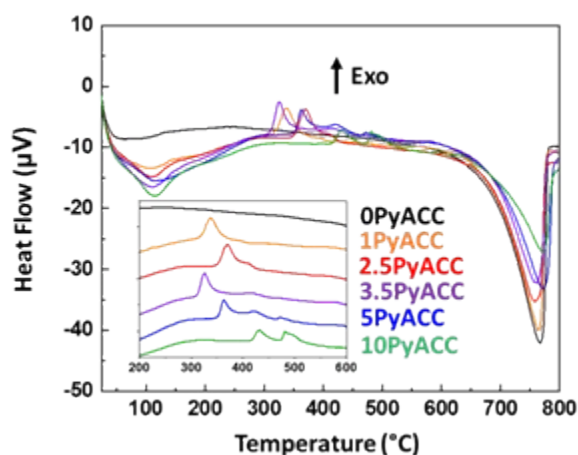
E. Differential Thermal Analysis

Figure S5: DTA curves of the synthesised zPyACC samples heated from 25°C to 800°C in air at a rate of 5°C/min. The curves are shifted in the inset for better clarity.

F. EDS mapping methodology and analysis movie

During the EDS analysis of the 5PyACC powder, the incident electron beam caused the water radiolysis as described by Du *et al.*[6] and the water contained in the nanoparticle transformed into water vapour and formed an entrapped bubble into the resin. We saw this bubble moving within the particle without any modification of the external shape of the latter, during the 6 min of EDS analysis. The attached movie was created by the succession of all of the 60 frames of the analysis. The dimensions of the picture are 130 nm x 130 nm.

Oxygen, phosphorus and calcium distributions into the 5PyACC particle determined by EDS analysis (Figures 5d, 5e, 5f) could appear inhomogeneous, unlike what we discussed in the main text of the article. In fact, calcium and oxygen seemed concentrated to the upper left part of the particle but it was related to the presence of the gas bubble at the bottom right and the low content of pyrophosphate. As EDS is also sensitive to the volume, for O and Ca we detected atoms from the upper surface of the spherical particle, but also from the lower surface after crossing the internal volume of the particle, except for the bottom right part that was masked by the gas bubble. But for P, as there was a lower content, with such a brief analysis (necessary to avoid strong alteration of the sample), we only collected the signal coming from the P atoms present at the upper surface of the particle, and not from the lower surface, leading to a distribution that appeared homogeneous despite the presence of the gas bubble.

G. SAXS fitting

The software SASView was used for fitting the SAXS curves. In this whole section, the uncertainties given are coming from the fitting process. To determine the first characteristic dimension D_1, two power law models with a $I(q) = k.q^{-p}$ equation type were created. The first power law, adjusted on the first 6 points of the curve, was $I_{pl1}(q) = 0.18q^{-2.114}$ for 10PyACC. The second one, adjusted to the main slope at the intermediate angles, was $I_{pl2}(q) = 4.98.10^{-5}q^{-3.9587}$. The intersection point of both lines was calculated at $q_1 = 0.0121$ Å^{-1}, *i.e.* with $q_1 = 2\pi/D_1$, $D_1 = 51.9 \pm 0.2$ nm. Then, in order to exacerbate the hump and make the fitting easier, the second power law $I_{pl2}(q)$ was subtracted to the data. The first

$$I_{Gp}(q) = k.exp\left[\dfrac{-\dfrac{1}{2}(q-q_0)^2}{\sigma^2}\right]$$

attempt for fitting was done using a Gaussian peak model , with the peak being centered at q_0 and having a standard deviation of σ. After an adjustment of the initial parameters by hand, the fitted parameters were R_{2Gp} = 3.38 $\pm$ 0.01 nm with σ = 0.03 for 10PyACC. The fitting was refined using a hardsphere structure factor added to a sphere model, to take into account the interactions between the close spheres. The equation, given in the Materials and Methods part, was applied with a scattering length density of calcite (for the clusters) of $2.57.10^{-5}$ Å^{-2} (really close to the vaterite one: $2.41.10^{-5}$ Å^{-2}) and of water of $9.48.10^{-6}$ Å^{-2}. After a manual adjustment of the initial parameters it gave the following fitted parameters for 10PyACC: $R_{2s.hs}$ = 2.485 $\pm$ 0.008 nm with a 14 % polydispersity, R_{2eff} = 3.70 $\pm$ 0.01 nm with a 10 % polydispersity and volume fraction = 0.697 $\pm$ 0.005. The effective radius R_{2eff} is the distance between the centre of the sphere and the centre of the distance between two spheres, *i.e.* 2 R_{2eff}, is equal to the distance between the centres of two-neighbour spheres. It was really close to the R_{2Gp} obtained with the Gaussian peak model; consequently, we concluded that the latter was taking into account a part of the sphere-sphere interactions and not strictly the cluster radius. That is why we decided to focus mainly on the $R_{2s.hs}$ value, obtained with the sphere model, probably more accurate for the clusters size.

For identifying the peaks present in the WAXS curves, the JCPDS data of calcite (00-005-0586), vaterite (hexagonal, 01-072-0506), aragonite (01-071-2392) and monohydrocalcite (01-076-7969) were used.

Their corresponding 2θ were converted in q values using the following equation: $q = \dfrac{4\pi \sin\theta}{\lambda}$ (with λ = 1.5 Å), then the curves were plotted and compared to the zPyACC WAXS2D curves. For clarity, we showed only the comparison with calcite and vaterite (the other crystalline phases having no common peaks).
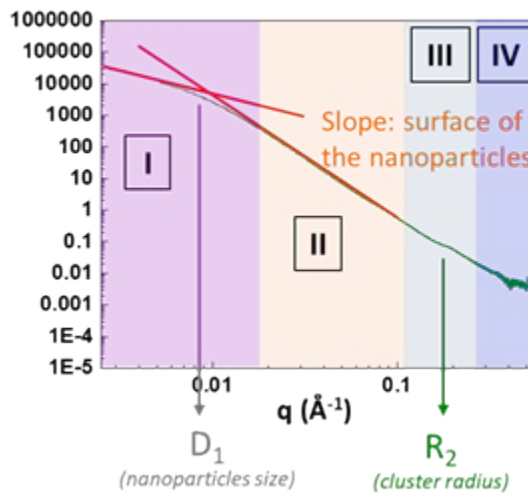

Figure S6: Explanation of the analysis method developed to fit the SAXS curves. The first dimension D_1 in the domain I can be calculated from the coordinates of the intersection point of the tangent to the curve (modelled by power laws). The slope in the domain II gave information on the nanoparticles surface. Then, the cluster radius R_2 in the domain III was obtained by fitting the hump.

H. Pair Distribution Function analysis

The reduced atomic PDF, G(r), gives, from a **structural model**, the probability of finding a pair of atoms at a distance r as follows:[7–12]

$$G(r) = 4.\pi. [\rho(r) - \rho_0]$$

where $\rho(r)$ is the atomic pair-density and ρ_0 is the average atomic number density.

As defined, peaks in the G(r) function correspond to specific distances separating a pair of atoms. G(r) can also be **extracted from an experimental XRD** pattern. Indeed, G(r) is the *sine* Fourier Transform of the reduced total scattering structure function F(Q):

$$F(Q) = Q.(S(Q)-1)$$

$$G(r) = \frac{2}{\pi} \int_{0}^{Qmax} Q.[S(Q) - 1].\sin(Q.r).dQ$$

where Q is the magnitude of the scattering vector ($Q = 4\pi \sin\left(\frac{\theta}{\lambda}\right)$), 2θ being the angle between the incoming and outgoing X-ray, λ is the X-ray wavelength, and S(Q) is the total scattering structure function which is the corrected and normalised experimental measured intensity.

Thus, PDF analysis provides information regarding inter-atomic distances leading to the local structure, for both crystalline and amorphous materials. When possible, the successful comparison between calculated and experimental G(r) leads to the structural modal validation.

SI-H1: Crystalline calcite and vaterite refinements.

Crystalline calcite and vaterite were synthesised as reference samples. Their local structures were refined allowing the cell parameters, isotropic atomic displacements, atomic positions and broadening factors to vary.

We used the Graf. D.L's published structure[13] for calcite. Concerning vaterite many structural models exist. We have carefully read Burgess[14] work who has been using DFT calculations, DRX and NMR data to compare all and select the two most probable structures. We attempted refinement from both models. The $P3_221$ model[15] presented a too high number of parameters to allow processing the refinement. We thus pursued our work with the C2 model[16] which allowed refinement using all parameters. This led to good reliability factors of 12.9 % for calcite and 10.9 % for vaterite, thus validating the structural models and our PDF setup.
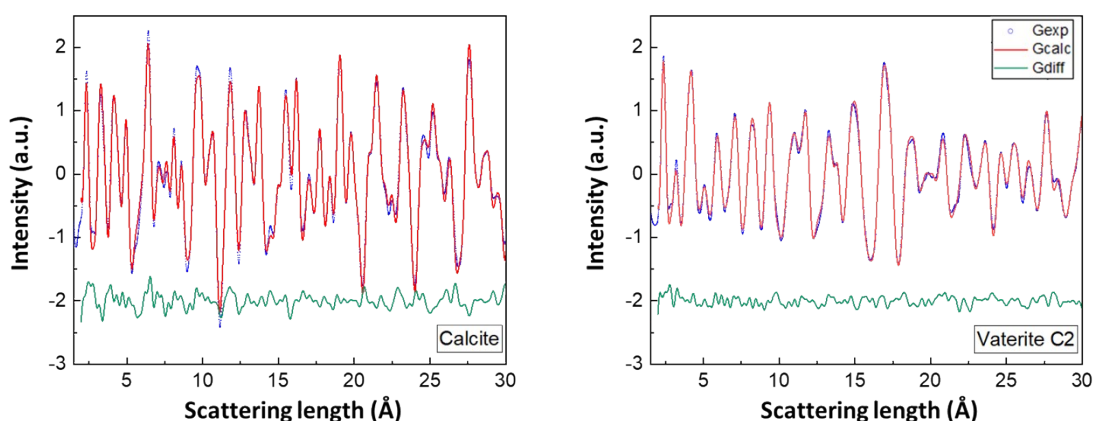
Figure S7: Experimental (blue circles), calculated (red line) and differential (green line) G(r) curves for calcite and monoclinic C2 vaterite

SI-H2: Experimental coherent length from PDF analysis

The coherence length, meaning the maximum distance for which the atoms are organised according to a single structure, could be determined from experimental PDF curve. This corresponded to the maximum r value for which PDF peaks could still be distinguished from the background oscillations, as illustrated in Figure S8. Table S1 presents the coherence length extracted from the PDF curves.

Table S1: Coherence length of the zPyACC determined by PDF analysis.

Samples	Coherence length (nm)
1PyACC	55-60
2.5PyACC	50-55
3.5PyACC	1
5PyACC	1
10PyACC	1

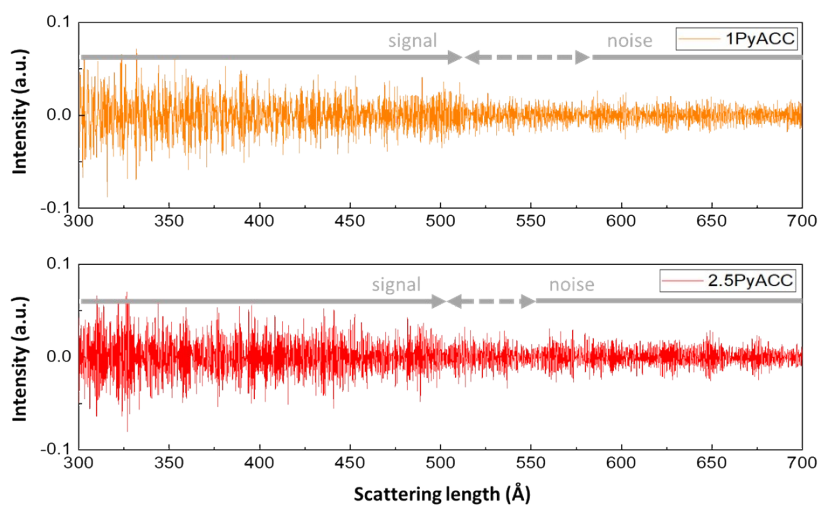*Figure S8: Experimental PDF curves (Gexp(r)) at larger r scales, for 1PyACC (top) and 2.5PyACC (bottom), showing their coherence length between 50 and 60 nm, above which the signal cannot be distinguished from the noise.*

7

SI-H3: Calculation of amorphous calcite and vaterite

Refined parameters from refined crystalline calcite and vaterite were used, combined with a dampening factor of 9 Å to mimic the absence of organisation at high distances in the amorphous phases. Even at small distances, amorphous calcite and amorphous vaterite had different signatures and thus could be distinguished (Figure S9).
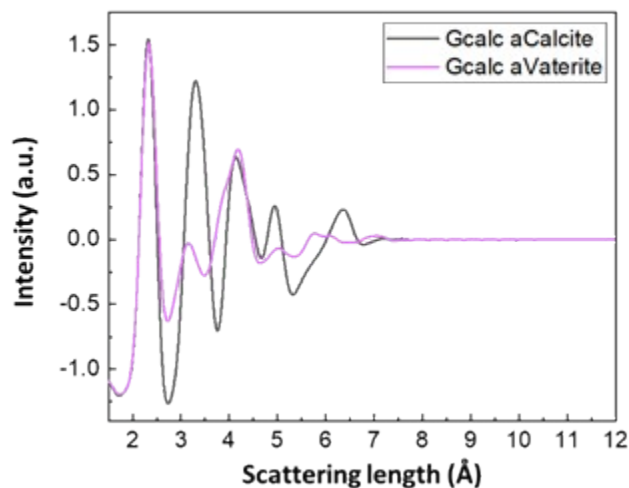

Figure S9: Comparison of the calculated PDF curves (Gcalc(r)) for amorphous calcite (aCalcite) and amorphous vaterite (aVaterite)

SI-H4: The amorphous phase in 1PyACC and 2.5PyACC samples

Both experimental 1PyACC and 2.5PyACC PDF curves only presented peaks at distances corresponding to calcite. However, intensities for 2.5PyACC sample declined faster with r that for the 1PyACC one or crystalline calcite, which made it harder to compare and interpret (Figure S10a). We normalised the three curves based on the 27.6 Å peaks. It showed that all samples presented the same structure, calcite, at high distances, but that an additional amorphous phase was also present at small order, below 9 Å (Figure S10b). Subtractions of the normalised curves ($G_{exp}(r)$1PyACC - $G_{exp}(r)$calcite and $G_{exp}(r)$2.5PyACC - $G_{exp}(r)$calcite) gave a similar signal (peaks at the same distances), with higher intensities for 2.5PyACC than for 1PyACC (Figure S10c). Normalisation based on the first peak showed that both normalised differences were equal, meaning that a similar amorphous phase (named a1PyACC and a2.5PyACC) was obtained in addition to crystalline calcite, when Py was present during precipitation (Figure S10d): the more Py initially in solution, the more amorphous phase was present in the synthesised powder.
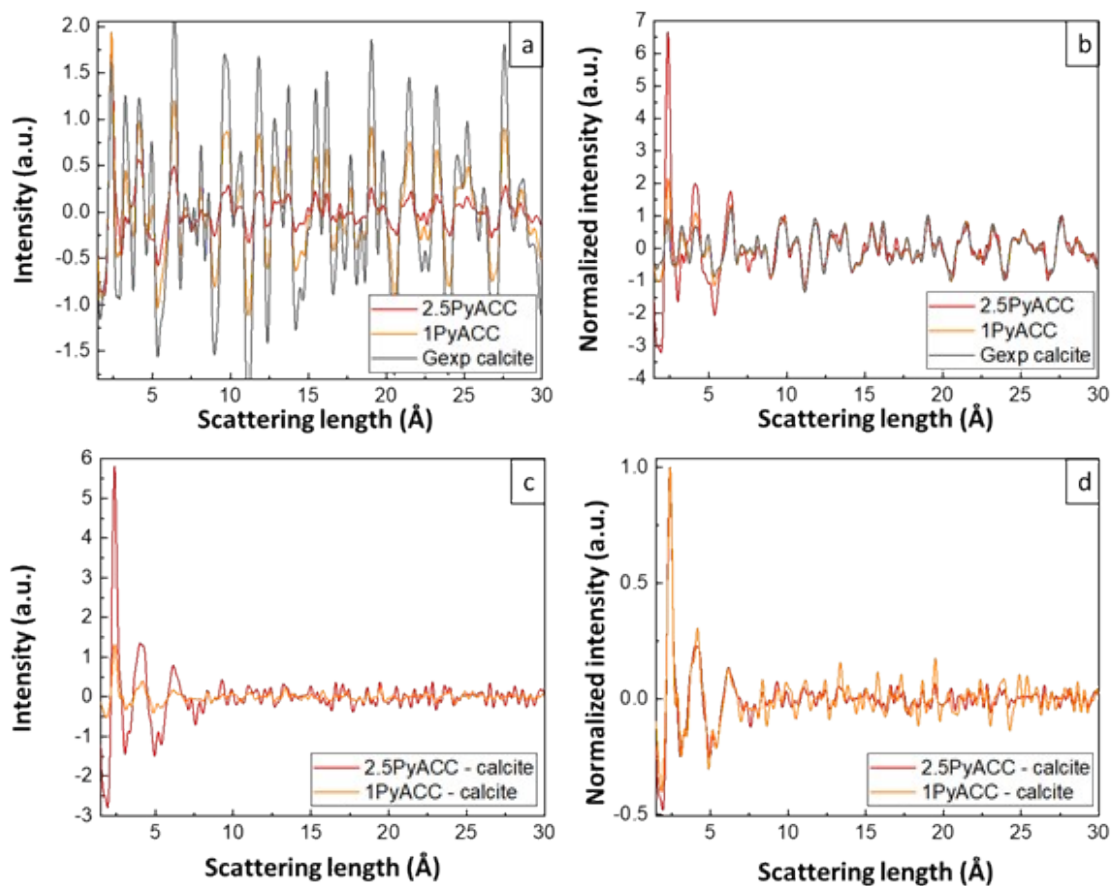
Figure S10: Comparison of the experimental Gexp(r) curves of 2.5PyACC, 1PyACC and calcite without normalisation (a) and after a normalisation by the 27.6 Å peak (b). Gexp(r)1PyACC - Gexp(r)calcite and Gexp(r)2.5PyACC - Gexp(r)calcite curves without additional normalisation (c) and with a normalisation by the first peak (d).

SI-H5: Comparison between amorphous calculated calcite and experimental amorphous 3.5PyACC, 5PyACC and 10PyACC

The amorphous 3.5PyACC, 5PyACC and 10PyACC Gexp(r) curves presented a large peak at 3.8 Å (blue arrow in Figure S11) that could not be reproduced with amorphous calculated calcite. Similarly, the intense peak at 3.3 Å of amorphous calculated calcite did not match with the amorphous 3.5PyACC, 5PyACC and 10PyACC Gexp(r) curves (grey arrow in Figure S11). We could not validate the calcite structure as a conceivable model.
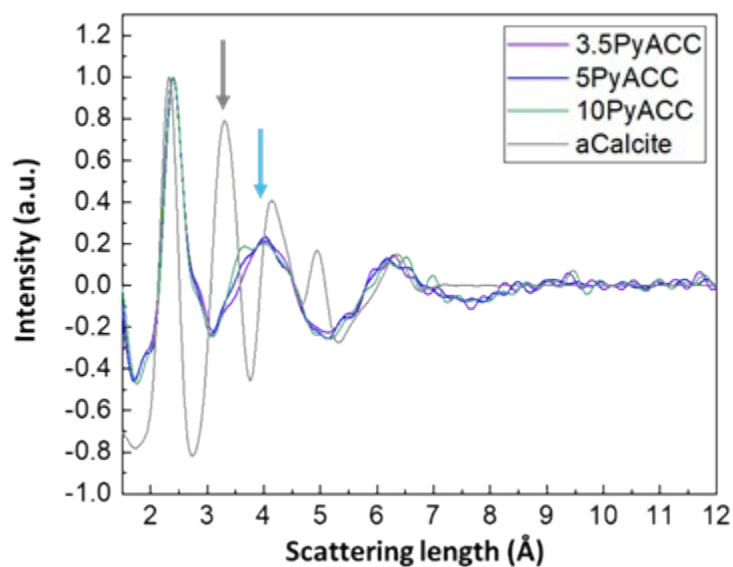
Figure S11: Comparison of the Gexp(r) of the fully amorphous zPyACC samples (3.5PyACC, 5PyACC and 10PyACC) and the Gcalc(r) of the amorphous calcite (aCalcite).

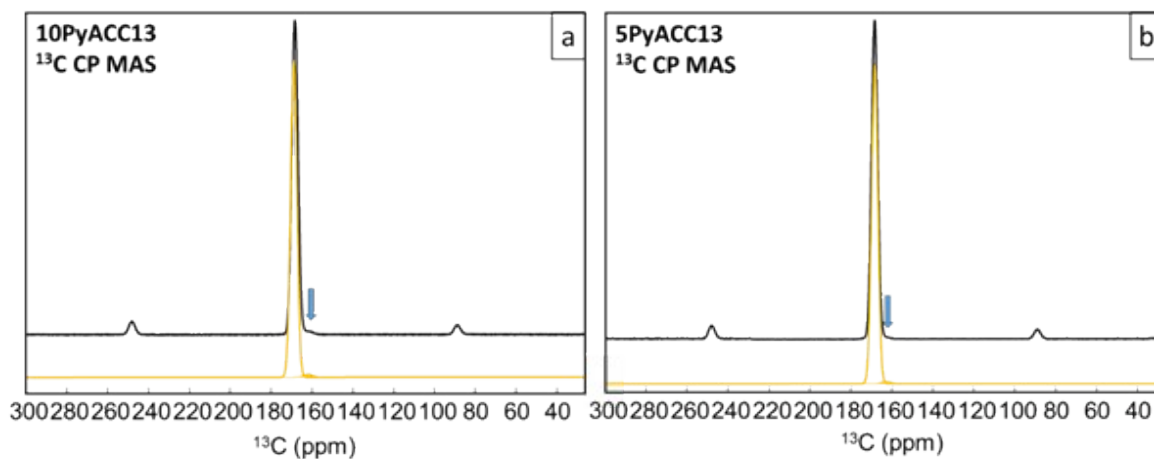I. NMR ^{13}C CP MAS spectra of 5PyACC13 and 10PyACC13 samples

*Figure S12: ^{13}C CP MAS spectra of 10PyACC13 **(a)** and 5PyACC13 **(b)**. The DMFit simulations are shown in orange. The major component corresponds to CO_3^{2-} species whereas the very minor one (plain, orange) corresponds to HCO_3^{-} species. The associated parameters are given in the main text.*

Bibliography

1   P. Gras, C. Rey, O. Marsan, S. Sarda and C. Combes, *Eur. J. Inorg. Chem.*, 2013, **2013**, 5886–5895.
2   C. Rey, O. Marsan, C. Combes, C. Drouet, D. Grossin and S. Sarda, in *Advances in Calcium Phosphate Biomaterials*, ed. B. Ben-Nissan, Springer Berlin Heidelberg, Berlin, Heidelberg, 2014, vol. 2, pp. 229–266.
3   B. Xu, A. Hirsch, L. Kronik and K. M. Poduska, *RSC Advances*, 2018, **8**, 33985–33992.
4   G. Behrens, L. T. Kuhn, R. Ubic and A. H. Heuer, *Spectroscopy Letters*, 1995, **28**, 983–995.
5   L. Mayen, N. D. Jensen, D. Laurencin, O. Marsan, C. Bonhomme, C. Gervais, M. E. Smith, C. Coelho, G. Laurent, J. Trebosc, Z. Gan, K. Chen, C. Rey, C. Combes and J. Soulié, *Acta Biomaterialia*, 2019, S1742706119308566.
6   H. Du, M. Steinacher, C. Borca, T. Huthwelker, A. Murello, F. Stellacci and E. Amstad, *J. Am. Chem. Soc.*, 2018, **140**, 14289–14299.
7   T. Egami and S. J. L. Billinge, *Underneath the Bragg Peaks: Structural Analysis of Complex Materials*, Newnes, 2012.
8   O. Masson and P. Thomas, *J Appl Cryst*, 2013, **46**, 461–465.
9   S. J. L. Billinge and M. G. Kanatzidis, *Chemical Communications*, 2004, **0**, 749–760.
10   V. Petkov, *Materials Today*, 2008, **11**, 28–38.
11   C. L. Farrow and S. J. L. Billinge, *Acta Cryst A*, 2009, **65**, 232–239.
12   M. W. Terban and S. J. L. Billinge, *Chem. Rev.*, 2022, **122**, 1208–1272.
13   D. L. Graf, *American Mineralogist*, 1961, **46**, 1283–1316.
14   K. M. N. Burgess and D. L. Bryce, *Solid State Nuclear Magnetic Resonance*, 2015, **65**, 75–83.
15   R. Demichelis, P. Raiteri, J. D. Gale and R. Dovesi, *CrystEngComm*, 2012, **14**, 44–47.
16   R. Demichelis, P. Raiteri, J. D. Gale and R. Dovesi, *Cryst. Growth Des.*, 2013, **13**, 2247–2251.